

IMPACT OF ATMOSPHERIC REFRACTION: HOW DEEPLY CAN WE PROBE EXO-EARTH'S ATMOSPHERES DURING PRIMARY ECLIPSE OBSERVATIONS?

YAN BÉTRÉMIEUX AND LISA KALTENEGGER¹

Max-Planck-Institut für Astronomie, Königstuhl 17, D-69117 Heidelberg, Germany; betremieux@mpia.de

Received 2013 December 23; accepted 2014 June 18; published 2014 July 21

ABSTRACT

Most models used to predict or fit exoplanet transmission spectra do not include all the effects of atmospheric refraction. Namely, the angular size of the star with respect to the planet can limit the lowest altitude, or highest density and pressure, probed during primary eclipses as no rays passing below this critical altitude can reach the observer. We discuss this geometrical effect of refraction for all exoplanets and tabulate the critical altitude, density, and pressure for an exoplanet identical to Earth with a 1 bar N_2/O_2 atmosphere as a function of both the incident stellar flux (Venus, Earth, and Mars-like) at the top of the atmosphere and the spectral type (O5–M9) of the host star. We show that such a habitable exo-Earth can be probed to a surface pressure of 1 bar only around the coolest stars. We present 0.4–5.0 μm model transmission spectra of Earth's atmosphere viewed as a transiting exoplanet, and show how atmospheric refraction modifies the transmission spectrum depending on the spectral type of the host star. We demonstrate that refraction is another phenomenon that can potentially explain flat transmission spectra over some spectral regions.

Key words: atmospheric effects – Earth – line: identification – methods: analytical – planets and satellites: atmospheres – radiative transfer

Online-only material: color figures

1. INTRODUCTION

The ongoing discovery of new exoplanets and its potential for finding other Earth-like planets has fueled studies (Ehrenreich et al. 2006; Kaltenegger & Traub 2009; Pallé et al. 2009; Vidal-Madjar et al. 2010; Rauer et al. 2011; García Muñoz et al. 2012; Snellen et al. 2013; Hedelt et al. 2013; Bétrémieux & Kaltenegger 2013; Rodler & López-Morales 2014; Misra et al. 2014) modeling the spectrum of the Earth's atmosphere viewed as a transiting exoplanet. However, most models predicting, or fitting, the spectral dependence of planetary transits have not fully included a fundamental phenomenon of the atmosphere on radiation: refraction. As light rays traverse an atmosphere, they are bent by refraction from the major gaseous species. The angular deflection is, to the first order, proportional to the density of the gas (Goldsmith 1963) so that the greatest ray bending occurs in the deepest atmospheric regions. This differential refractive bending of light with altitude generally decreases the flux of a point source when observed through an atmosphere. Combined with absorption and scattering from gas and aerosols, it has been used to interpret stellar occultation by planetary atmospheres in our solar system to determine their composition with altitude (see, e.g., Smith & Hunten 1990 and references therein).

In an exoplanetary transit geometry, where the star is an extended source with respect to the observed planetary atmosphere and the observer is infinitely far away, refraction produces different effects. Right before and after a transit, some stellar radiation can bend around through the deeper regions of the planet's opposite limb, toward the observer, while the stellar disk is unocculted. This results in a global flux increase if the atmosphere is not opaque (Sidis & Sari 2010). Conversely, during transit,

refraction from the deeper atmospheric regions deflects light away from the observer. The latter effect can limit how deeply atmospheres can be probed during exoplanetary transits. Indeed, when the angular extent of the star with respect to the planet is sufficiently small, rays traversing a planetary atmosphere below a critical altitude will be bent so much that no rays from the stellar surface can reach the distant observer. This effect masks molecular absorption features that originate below this altitude. Whereas refractive effects have been shown not to be important for hot giant exoplanets (see the analysis of HD 209458b by Hubbard et al. 2001) and the high-altitude hazes and clouds in the Venusian atmosphere are located above the critical altitude of a Venus–Sun analog (García Muñoz & Mills 2012), for an Earth–Sun analog, the critical altitude occurs in the upper troposphere, above the cloud deck, and the strength of water absorption features are substantially reduced (García Muñoz et al. 2012; Bétrémieux & Kaltenegger 2013).

How deeply can we probe the atmospheres of Earth-like planets in transit around other stars? For which stellar spectral types can one probe down to the planetary surface? What impact does it have on the spectral features of an exo-Earth during primary eclipse observations? In this paper, we address these questions for an exo-Earth, a planet defined here as having the same mass and radius and an identical 1 bar N_2/O_2 atmosphere as the Earth. We explore how the critical altitude changes with spectral type, along the main sequence, of the host star (O5–M9), modifying the planet–star distance to keep the incident stellar flux constant for fluxes between that of present-day Venus and Mars. We first discuss the basic effects of refraction in an exoplanet transit geometry (Section 2); present our refraction model and our results (critical altitudes, densities, and pressures) around various stars (Section 3); and then show the impact on an exo-Earth's transmission spectrum from 0.4 to 5.0 μm (Section 4), a spectral region relevant to the *James Webb Space Telescope* as well as ground-based observatories such as E-ELT.

¹ Also at Harvard-Smithsonian Center for Astrophysics, 60 Garden Street, Cambridge, MA 02138, USA.

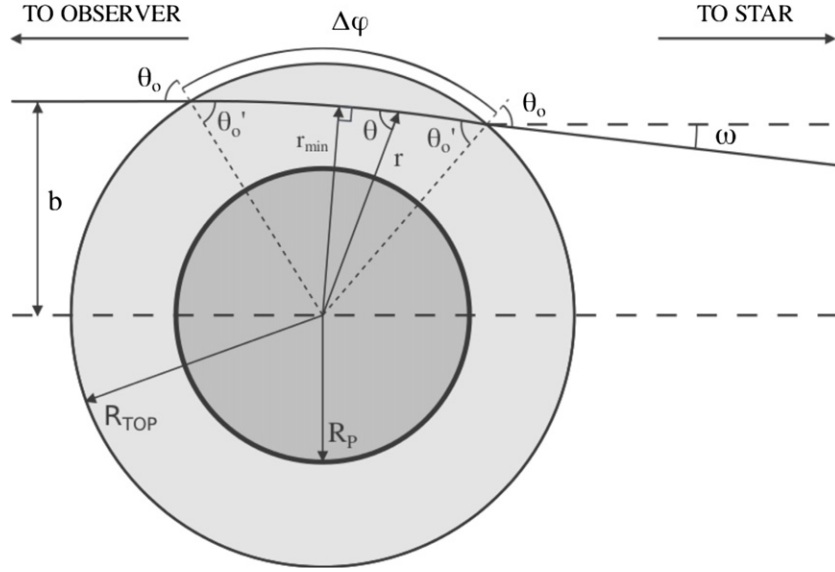


Figure 1. Bending of the light ray by atmospheric refraction for an exoplanetary transit. The planetary body (dark gray) and the atmosphere (light gray) are shown along with the observer-to-planet-center axis (dashed line) with the observer to the left and the star to the right. The radius of the planetary surface, R_p ; the top of the atmosphere, R_{top} ; and the zenith angle, θ , of the ray for a given radial position, r , are also indicated. A light ray observed with an impact parameter, b , reached a minimum radial position r_{min} and is deflected by ω by the atmosphere.

2. REFRACTION THEORY FOR EXOPLANET TRANSIT GEOMETRIES

2.1. Atmospheric Refraction

The exponentially increasing density, and hence refractivity, of the atmosphere with depth causes light rays to bend toward the surface as they traverse the atmosphere (see Figure 1). Rays follow a path described by an invariant $L = (1 + \nu(r))r \sin \theta(r)$, where both the zenith angle of a ray, $\theta(r)$, and the refractivity of the atmosphere, $\nu(r)$, are functions of the radial position of the ray with respect to the center of the planet. The refractivity of the atmosphere depends on its composition, and is given by

$$\nu(r) = \left(\frac{n(r)}{n_{STP}} \right) \sum_j f_j(r) \nu_{STPj} = \left(\frac{n(r)}{n_{STP}} \right) \nu_{STP}(r), \quad (1)$$

where $n(r)$ is the number density, n_{STP} is the number density at standard temperature and pressure (STP) also known as Loschmidt's number, $f_j(r)$ is the mole fraction of the j th species, ν_{STPj} is the STP refractivity of the j th species, while $\nu_{STP}(r)$ is the STP refractivity of the atmosphere. Note that the ratio inside the parenthesis in Equation (1) is the number density expressed in units of amagat, which we will use throughout the paper. Assuming the refractivity just outside the atmosphere is zero, we can relate the lowest altitude reached by a ray, Δz_{min} , to its impact parameter, b . From the conservation of the invariant L , as well as the geometry in Figure 1 combined with Snell's law,

$$r_{min} = \Delta z_{min} + R_p \quad (2a)$$

$$L = (1 + \nu(r_{min}))r_{min} = (1 + \nu(R_{top}))R_{top} \sin \theta'_0 \quad (2b)$$

$$b = R_{top} \sin \theta_0 = (1 + \nu(R_{top}))R_{top} \sin \theta'_0, \quad (2c)$$

we can see that the impact parameter is equal to the ray invariant L . Here, R_{top} is the radius of the top of the atmosphere, R_p is the radius of the planetary surface, r_{min} is the lowest radial position reached by a ray, while θ_0 and θ'_0 are the zenith angle

of the ray just outside and inside the top atmospheric boundary, respectively (see Figure 1).

The deflection of the ray, ω , expressed in radian, is given by

$$\omega = \Delta\phi + 2\theta_0 - \pi, \quad (3)$$

where $\Delta\phi$ can be described as an angular travel of the ray through the atmosphere. For a simple homogeneous isothermal atmosphere, Goldsmith (1963) showed that to the first order, the deflection of the ray is given by

$$\omega = \left(\frac{2\pi r_{min}}{H(\Delta z_{min})} \right)^{1/2} \nu_{STP}(\Delta z_{min}) n(\Delta z_{min}), \quad (4)$$

where H is the atmospheric density scale height. Since the density decreases exponentially with altitude, the ray deflection is very sensitive to the lowest altitude reached and thus to the impact parameter of the ray. Note that since most atmospheres are far from isothermal, we use a ray-tracing algorithm (see Section 3.1 and Bétrémieux & Kaltenegger 2013) to compute the atmospheric deflection.

2.2. Critical Deflection of a Planet–Star System

The exoplanet transit geometry is exactly the reverse of the stellar occultation geometry. In stellar occultations, the source is infinitely far away from the refractive medium, or planetary atmosphere, while the observer is relatively close. In exoplanet transits, the observer is infinitely far away while the source is relatively close to the atmosphere. In this geometry, where all the rays reaching the observer are parallel with varying impact parameters, refraction produces three effects. The most obvious effect, also present in stellar occultations, is an increase in the optical depth due to an increase in the ray's path length through the atmosphere as the ray is bent. Previous calculations usually incorporate this effect when refraction is said to be included (see, e.g., Kaltenegger & Traub 2009; Benneke & Seager 2012). The second effect comes from the mapping of r_{min} into b . As we can see from Equations (2b) and (2c), b is always larger than r_{min} . The difference between the two quantities increases

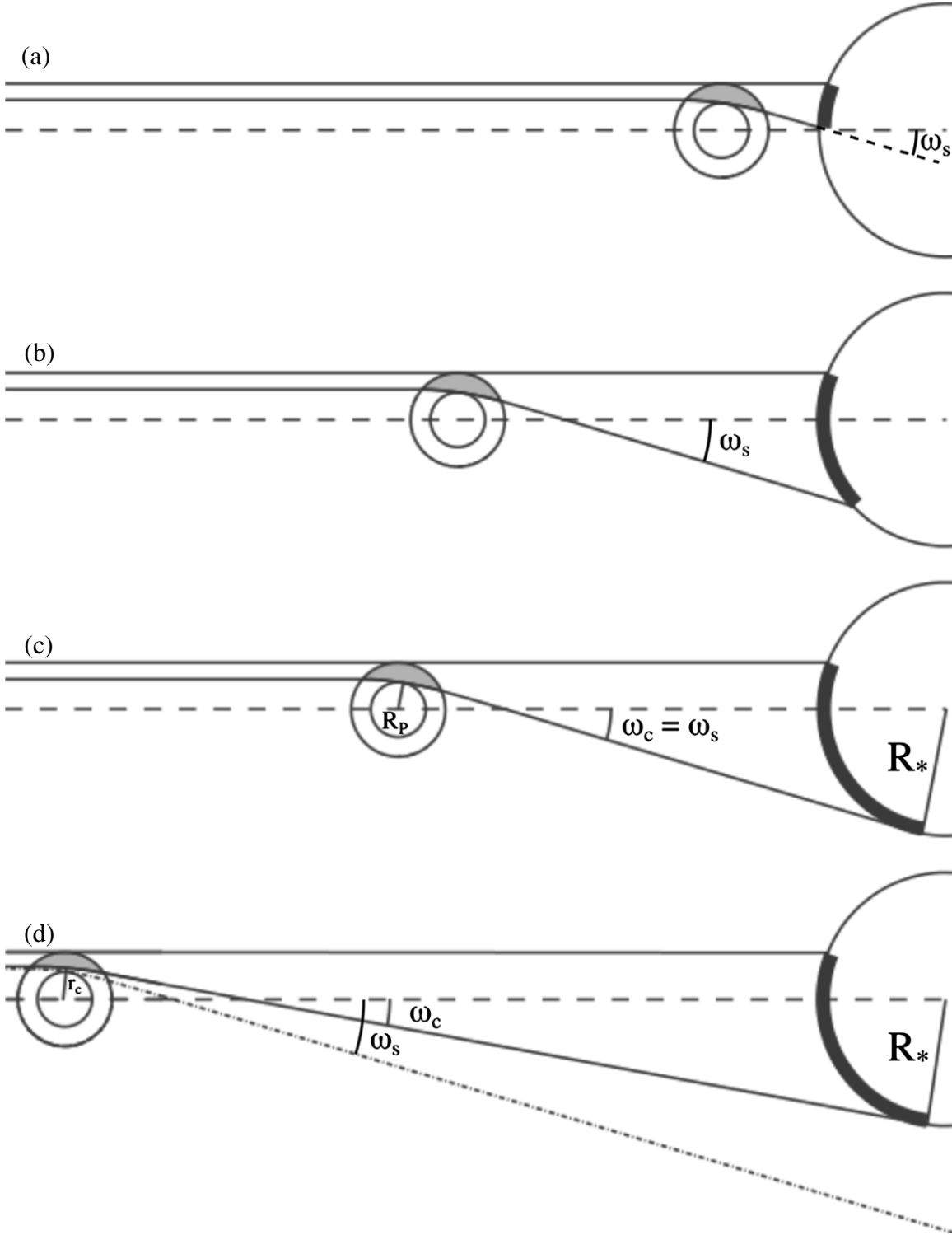


Figure 2. Geometry of exoplanetary transits with increasing planet–star distance. Two solid lines joining the star (right) to the observer (left along the dashed line) define the envelope of rays that can be seen by the observer through one exoplanetary limb. Shaded areas show the atmospheric region that can be probed by the observer, while the thick circumference shows the stellar region where the rays come from. The stellar radius, R_* ; radius of planetary surface, R_p ; critical radius, r_c ; surface deflection, ω_s ; and critical deflection, ω_c , are indicated. With short planet–star distances, light rays come from a stellar region behind the planet (a). As the planet–star distance increases, some rays come from the region of the star beyond the planet’s opposite limb (b). At a critical planet–star distance, rays grazing the planetary surface come from the star’s opposite limb (c). For larger planet–star distances, only rays that traverse the atmosphere above a critical altitude can reach the observer and lower atmospheric regions cannot be probed (d).

with refractivity, or decreasing altitude. The largest difference exists for the rays grazing the planetary limb ($r_{\min} = R_p$), thus the planet appears slightly larger to a distant observer. This second effect should be implicitly included with the first when

optical depth calculations are done as a function of b rather than r_{\min} .

The third effect, illustrated in Figure 2 for the cylindrically symmetric case when the planet occults the central region of

its star, is a purely geometrical effect linked to the angular size of the host star with respect to the planet, and it has only been included in a few papers (García Muñoz & Mills 2012; García Muñoz et al. 2012; Bétrémieux & Kaltenegger 2013; Rodler & López-Morales 2014; Misra et al. 2014). At the top of the atmosphere, the ray from the star is undeflected. As the impact parameter of the rays decreases, the deflection of the rays increases. A maximum deflection occurs for rays that graze the planetary surface. Although the deflection is small, the planet–star distance is large, so that the lateral displacement of the rays is significant. If the planet is sufficiently close to its star or the atmosphere is sufficiently tenuous, rays reaching the observer after passing through the planetary atmosphere merely come from a wider annular region on the stellar surface than the simple projection of the planetary atmosphere on the star would suggest (see Figure 2(a)). As the distance between the planet and the star increases, the inner edge of this region moves toward and eventually crosses the center of the star, and continues further on radially outward. Eventually, this edge can move beyond the projection of the opposite limb of the planet on the stellar surface (Figure 2(b)). At a critical planet–star distance, rays grazing the planetary surface reach the opposite limb of the star (Figure 2(c)). If the planet orbits beyond this critical distance, then only rays above a critical altitude can traverse the atmosphere and reach the observer (Figure 2(d)). Atmospheric regions below that altitude cannot be probed, therefore the planet will seem larger than it is. Atmospheric opacity does limit the depth that can be probed as well, but for the sake of brevity, we only refer to the effect from refraction throughout this paper unless specified otherwise. Note that in Section 4, we present all effects, not only refraction, and therefore produce the transmission spectrum of Earth seen as an exoplanet in transit around different host stars.

Whether the lower atmospheric regions are dark due to this refraction effect or because these regions are intrinsically opaque makes no difference to the transmission spectrum. Refraction does not change the transmission spectrum of an Earth–Sun analog shortward of $0.4 \mu\text{m}$ because of the high opacity of the atmosphere in the ultraviolet (Bétrémieux & Kaltenegger 2013). Figure 2 shows that stellar limb darkening effects will probably be different from what has previously been modeled because the stellar region of origin of the rays is not merely the projected limb of the atmosphere on the star. This could explain part of the discrepancy between theoretically derived limb darkening coefficients and those inferred through light curve fitting (see discussion in Csizmadia et al. 2013 for other explanations). However, to focus on the effects of refraction, we ignore limb darkening in this paper and assume that the specific intensity across the stellar disk is uniform.

One can calculate the critical deflection, ω_c , undergone by a ray that reaches the opposite stellar limb if one assumes that all of the bending of the ray occurs at the minimum altitude reached by the ray. Given that the path length of the ray through the atmosphere is much smaller than the planet–star distance, d , and that the curvature of that path is very small, this approximation introduces negligible errors when computing the total lateral displacement of the beam at the star’s position. In that case, from the geometry in Figure 2(d), we can see that

$$\sin \omega_c = \frac{r_c + R_*}{d} = \frac{(R_p + \Delta z_c) + R_*}{d} \approx \frac{R_p + R_*}{d}, \quad (5)$$

assuming that the critical altitude, Δz_c , is much smaller than the sum of the planetary surface radius, R_p , and the stellar radius,

R_* . The critical altitude is then defined as the altitude at which the atmospheric ray deflection, dependent on the atmospheric properties and size of the exoplanet (Equation (4)), matches the critical deflection of the planet–star system. The critical density and critical pressure are the number density and pressure of the atmosphere at the critical altitude, respectively. Note that when $R_p \ll R_*$, Equation (5) reduces to the expression for the angular radius of the star with respect to the planet. The critical deflection is mostly sensitive to the R_*/d ratio and does not strongly depend on the atmospheric properties of the exoplanet. A change in planetary radius from $1 R_\oplus$ (Earth) to $2 R_\oplus$ (super-Earth) changes the critical deflection by about 1% around a Sun-like star and about 10% around an M9 star.

The assumed geometry is only strictly valid when the observer, planet, and star are perfectly aligned. Deviation from this alignment during the course of a transit breaks the symmetry of the two opposing limbs, where radiation going through one limb can penetrate deeper than in the opposite one. Just outside of transit (OT), the planetary limb toward the star cannot be probed at all, while the critical deflection for the opposite limb, ω_{cOT} , increases to

$$\sin \omega_{cOT} = \frac{r_c + R_{\text{top}} + 2R_*}{d} \approx \frac{2R_p + 2R_*}{d} = 2 \sin \omega_c. \quad (6)$$

Only a detailed study of the refraction effect on the full exoplanetary transit light curve will reveal to what extent this modifies the wings of the transit light curve. For this paper, we will use this simpler geometry as an average representation to discuss the first-order effects of refraction on the exoplanetary transmission spectrum.

2.3. Dependence of Critical Deflection with Stellar Spectral Type

The wavelength-integrated stellar flux, F_* , on the top of a planetary atmosphere is given in a first-order approximation assuming the star to be a blackbody by

$$F_* = \sigma T_*^4 \left(\frac{R_*}{d} \right)^2, \quad (7)$$

where T_* is the stellar effective temperature, and σ is the Stefan–Boltzmann constant. Hence, the planet–star distance, d , at which the stellar flux on top of an exoplanet’s atmosphere equals that of a solar system planet at a distance d_\odot , is given by

$$\frac{d}{d_\odot} = \left(\frac{R_*}{R_\odot} \right) \left(\frac{T_\odot}{T_*} \right)^2, \quad (8)$$

where here, the subscript \odot refers to quantities for our solar system.

Using Equations (5) and (8), the critical deflection around other stars can be related to that of planets in our solar system, $\omega_{c\odot}$, by

$$\begin{aligned} \frac{\sin \omega_c}{\sin \omega_{c\odot}} &= \left(\frac{R_p + R_*}{R_p + R_\odot} \right) \left(\frac{d}{d_\odot} \right)^{-1} \\ &= \left[\left(\frac{R_p + R_*}{R_p + R_\odot} \right) \left(\frac{R_\odot}{R_*} \right) \right] \left(\frac{T_\odot}{T_*} \right)^2. \end{aligned} \quad (9)$$

The ratio inside the square bracket simplifies to unity when $R_p \ll R_*$. Even in the case of an Earth-sized planet around

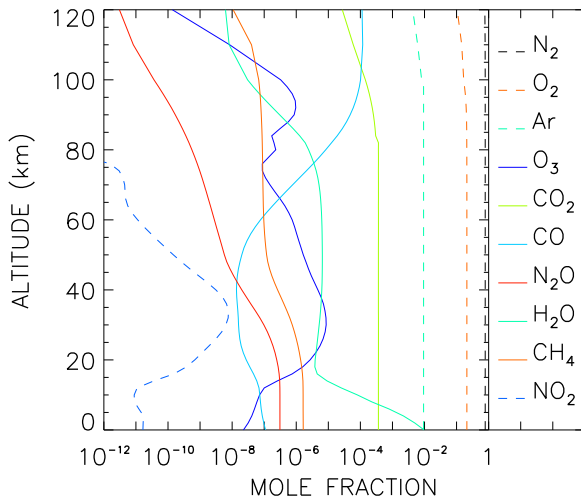


Figure 3. Composition of the Earth’s atmosphere as a function of altitude for solar minimum conditions (see Bétrémieux & Kaltenegger 2013).

(A color version of this figure is available in the online journal.)

an M9 star, the ratio is still 1.10, fairly close to unity. Thus, in the small angle approximation and for $R_p \ll R_*$, Equation (9) simplifies to

$$\frac{\omega_c}{\omega_{c\odot}} \simeq \left(\frac{T_\odot}{T_*} \right)^2 \quad (10)$$

and is independent of stellar radius. Hence, for exoplanets with the same incident stellar flux, the critical deflection of the planet–star system is larger around cooler stars and deeper regions of the planetary atmosphere can be probed.

Note that Equation (10) is not used to determine the critical deflections of the planet–star system from which the critical altitudes presented in Section 3.2 are derived. Rather, we first use Equation (8) to compute the planet–star distance and then Equation (5) to determine the corresponding critical deflection. All of the atmosphere can be probed when the critical deflection of the planet–star system exceeds the ray deflection at the surface of the planet.

3. CRITICAL ALTITUDES AND DENSITIES

3.1. Model Description

To compute the refractive and absorptive properties of an exo-Earth, we use the disk-averaged Earth solar minimum model atmosphere and the ray tracing and radiative transfer model described in Bétrémieux & Kaltenegger (2013). This model traces rays through a spherical atmosphere discretized in 0.1 km thick homogeneous layers and computes $\Delta\phi$ from which the deflection is derived with Equation (3). This is done as a function of the minimum altitude reached by the ray, Δz_{\min} , from which b is computed with Equations (2a), (2b), and (2c). The model also computes column abundances and average mole fractions for different species along the path of the ray from which the optical depth and the transmission are derived. In this paper, the top of the atmosphere, R_{top} , is chosen 120 km above R_p where atmospheric absorption and refraction are negligible across our spectral region of interest (0.4–5 μm). The composition of Earth’s atmosphere with altitude is shown in Figure 3. The main refractors in the Earth’s atmosphere are N_2 , O_2 , Ar, and CO_2 , which make up more than 99.999% of the atmosphere. Although we include all these in our model, ignoring Ar and CO_2 would create less than a 1% change in the refractivity and hence

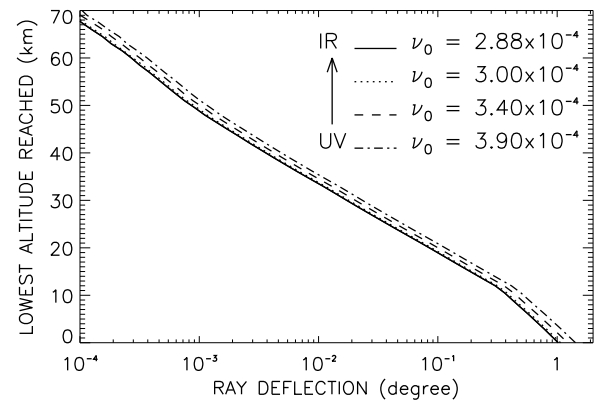


Figure 4. Ray deflection caused by atmospheric refraction as a function of the lowest altitude reached by that ray. The various curves show results for a sample of STP refractivities of Earth’s atmosphere, ν_{STP} , from the ultraviolet to the infrared, assumed to be constant with altitude (see the text).

on ray deflection. The contribution from water vapor is even smaller and is ignored here. Since the main refractors are well mixed throughout the atmospheric region considered, the STP refractivity hardly changes with altitude and is assumed to be the planet’s surface value, ν_{STP} , at all altitudes throughout our calculations.

As the STP refractivity varies with wavelength, the ray deflection and critical altitude will also be wavelength dependent. However, ν_{STP} changes only slightly in the infrared (IR), going from 2.8798×10^{-4} at 30 μm to 2.88×10^{-4} at 8.8 μm . Its variation with wavelength, although greater, is still small from the infrared to the near-infrared (NIR) and the visible (VIS). ν_{STP} is 2.90×10^{-4} at 0.87 μm and 3.00×10^{-4} at 0.37 μm . In the ultraviolet (UV), ν_{STP} changes more rapidly, reaching 3.40×10^{-4} at 0.20 μm , and becomes larger than 3.90×10^{-4} for wavelengths shorter than 0.14 μm . Figure 4 shows the ray deflection as a function of the lowest altitude reached by a ray for different ν_{STP} spanning values covering the IR to the UV. The difference in the STP refractivity from the IR to the UV changes the lowest altitude reached by rays, which have undergone the same deflection, by about 2 km for atmospheric regions above 12 km and about 3.5 km closer to the surface. The difference in the STP refractivity across our spectral region of interest (IR-VIS) induces a change in a ray’s minimum altitude of only about 0.25 km, most of which occurs across the visible. Since that difference is small, we will use a single value of 2.88×10^{-4} for ν_{STP} throughout the rest of the paper. Note that for this refractivity value, using Equation (4) instead of our ray-tracing model underestimates the ray deflection by up to approximately 4% near the surface while it overestimates it by an average of 7% above 10 km altitude. Even though the difference between the simplified isothermal treatment and our ray tracing model is small in this particular case, the ray-tracing model is still preferable on physical grounds.

3.2. Results

To determine around which spectral type stars the atmosphere of a habitable exo-Earth can be probed down to the surface, we must first determine the critical deflection of the exo-Earth–star system. We compute the critical deflection of an Earth-sized planet ($R_p = 6371$ km) orbiting various stars along the main-sequence track using Equations (5) and (8). The radius and effective temperature of the stars considered are listed in Table 1. We do the calculations for planets that receive the same stellar

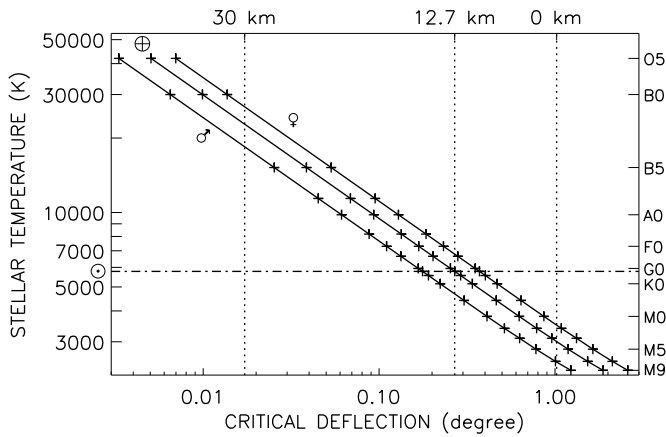


Figure 5. Critical deflection, ω_c , as a function of effective stellar temperature, T_* , for an Earth-sized exoplanet orbiting a main-sequence star (O5–M9). The three tracks, from left to right, show results for an exoplanet that is at a distance from its star where it receives the same stellar flux as present-day Mars, Earth, and Venus, respectively. Crosses show data points listed in Table 1, with our Sun’s temperature highlighted by the dot–dashed line. Vertical dotted lines show the deflection at Earth’s surface at 12.7 and 30 km altitudes. Only for critical deflections greater than or equal to that of the 0 km line can observers probe down to the exo-Earth’s surface.

flux as Earth ($d_\odot = 1$ AU) and contrast them with planets which receive the same stellar flux as Venus ($d_\odot = 0.723$ AU) and Mars ($d_\odot = 1.524$ AU). The results are shown in Figure 5 along with the ray deflection for three benchmark altitudes on Earth: that of the surface (0 km), the Earth–Sun critical altitude (12.7 km; see Bétrémieux & Kaltenegger 2013), and at 30 km, close to the peak of the ozone vertical profile. Transmission spectroscopy can probe the atmosphere of an exo-Earth down to its surface for stars that are cooler than or the same temperature as the limit defined by the surface ray deflection. This limit occurs for M1, M4, and M7 stars for Venus-like, Earth-like, and Mars-like fluxes, respectively. Hence, for main-sequence stars, observers can probe an exo-Earth to a surface pressure of 1 bar only around M dwarfs. For thinner N_2/O_2 atmospheres, this limit shifts to hotter stars, while for thicker N_2/O_2 atmospheres, it shifts to cooler stars.

For each exo-Earth–star system with a specified incident stellar flux (Venus, Earth, or Mars-like), we determine the critical altitude, density, and pressure by first computing the atmospheric deflection as a function of a ray’s minimum altitude on a 1.5 km altitude grid, and then determine which region produces deflections closest to the system’s critical deflection. We redo this step with successively finer altitude grids across the atmospheric region that has deflections closest to the critical deflection until we get to a 0.001 km grid. We then determine which altitude on that grid produces a deflection closest to the system’s critical deflection. The critical density and critical pressure are the number density and pressure of the atmosphere at this critical altitude, respectively.

As can be seen in Table 2, whereas an exo-Earth’s surface conditions can be probed around some of the cooler M dwarfs, the critical altitude increases as one observes planets around hotter stars, and the corresponding critical density and pressure decrease. For an Earth–Sun analog, most of the troposphere is inaccessible to observers. Although tropospheric water content cannot be determined, this also means that tropospheric clouds have no impact on the transmission spectrum and hence they cannot be responsible for transmission light curve variability. For stars hotter than B0 stars, the critical altitude lies even above 30 km and only the mesosphere and thermosphere can

Table 1
Effective Temperature and Radius of Main-sequence Stars

Stellar Spectral Type	T_* (K)	R_*/R_\odot
O5	42000	12.0
B0	30000	7.4
B5	15200	3.9
B8	11400	3.0
A0	9790	2.4
A5	8180	1.7
F0	7300	1.5
F5	6650	1.3
G0	5940	1.1
☉ - G2	5778 ^a	1.0
G5	5560	0.92
K0	5150	0.85
K5	4410	0.72
M0	3800	0.62
M2	3400	0.44
M4	3100	0.26 ^b
M5	2800	0.20
M7	2500	0.12
M9	2300	0.08

Notes. Source: Reid & Hawley (2005) for M stars, Cox (2000) otherwise.

^a Lodders & Fegley (1998).

^b Kaltenegger & Traub (2009).

be probed. For a given star, the critical altitude decreases as the stellar flux received by the exo-Earth increases because the star’s angular size with respect to the planet is larger. Although it is unclear at this point whether a planet in the habitable zone of O and B stars could, because of the extreme UV environment or the short lifetime of these stars, ever develop a stable atmosphere, we have nevertheless included the calculations for exo-Earths orbiting these stars to show what the extreme values are.

3.3. Effects of Different Atmospheric Profiles

Although differences in the spectral energy distribution of stars lead to differences in the thermal and chemical composition profile of an exoplanet’s atmosphere (see, e.g., Rugheimer et al. 2013), we use an Earth profile here to focus only on the geometrical effect of refraction. Hence, the values in Table 2 illustrate only the impact of refraction. Increasing the proportion of UV flux would increase the photodestructive rate of N_2 and O_2 in the thermosphere, where densities are low and refraction is not important. In the lower atmosphere, we expect no changes in the abundances of N_2 and O_2 because convection would replenish any altitude-localized depletion. Thus, v_{STP} would not change significantly in the lower atmosphere. However, increasing UV fluxes also increases the amount of ozone produced in the stratosphere with a resulting increase in stratospheric temperatures. Increasing visible and infrared flux increases the temperature in the troposphere. Hence, as the peak of the stellar spectral energy distribution shifts toward shorter wavelengths (i.e., hotter stars), stratospheric temperatures increase while tropospheric temperatures decrease. Since the ray deflection is sensitive mostly to the density of the lowest altitude reached by the ray, when the scale height doubles, the altitude that produces a given ray deflection will also double. Hence, the critical altitude scales with scale height. A second-order effect arises because $\omega \propto H^{-1/2} \approx T^{-1/2}$ (for isothermal region of atmosphere). As T increases, ω decreases and the critical altitude decreases slightly. Therefore, as T increases, the critical

Table 2
Exo-Earth Critical Altitude, Density, and Pressure versus Stellar Spectral Type

Stellar Spectral Type	Critical Altitude (km) for Same Incident Flux as			Critical Density (amagat) for Same Incident Flux as			Critical Pressure (mbar) for Same Incident Flux as		
	Venus	Earth	Mars	Venus	Earth	Mars	Venus	Earth	Mars
O5	35.7	37.9	40.6	5.84×10^{-3}	4.23×10^{-3}	2.84×10^{-3}	5.17	3.84	2.65
B0	31.5	33.6	36.2	1.13×10^{-2}	8.19×10^{-3}	5.46×10^{-3}	9.54	7.06	4.85
B5	22.9	24.9	27.5	4.34×10^{-2}	3.16×10^{-2}	2.09×10^{-2}	35.3	26.0	17.3
B8	19.3	21.3	23.9	7.70×10^{-2}	5.56×10^{-2}	3.67×10^{-2}	61.9	45.0	30.1
A0	17.3	19.4	22.0	1.05×10^{-1}	7.56×10^{-2}	4.96×10^{-2}	84.0	60.7	40.2
A5	15.1	17.1	19.8	1.49×10^{-1}	1.08×10^{-1}	7.10×10^{-2}	120	87.1	57.1
F0	13.6	15.7	18.3	1.86×10^{-1}	1.36×10^{-1}	8.95×10^{-2}	150	109	71.9
F5	12.5	14.5	17.1	2.24×10^{-1}	1.63×10^{-1}	1.08×10^{-1}	180	131	86.6
G0	11.1	13.1	15.7	2.80×10^{-1}	2.04×10^{-1}	1.35×10^{-1}	225	164	108
☉ - G2	10.2	12.7	15.4	3.10×10^{-1}	2.15×10^{-1}	1.42×10^{-1}	255	173	114
G5	9.44	12.2	14.9	3.43×10^{-1}	2.32×10^{-1}	1.54×10^{-1}	288	187	123
K0	7.99	11.3	13.9	4.07×10^{-1}	2.70×10^{-1}	1.79×10^{-1}	357	217	144
K5	4.90	8.08	12.0	5.76×10^{-1}	4.03×10^{-1}	2.43×10^{-1}	548	353	195
M0	1.78	5.15	9.24	7.96×10^{-1}	5.61×10^{-1}	3.51×10^{-1}	817	530	297
M2	0.00	2.79	7.06	9.48×10^{-1}	7.12×10^{-1}	4.53×10^{-1}	1013	720	407
M4	0.00	0.66	5.09	9.48×10^{-1}	8.89×10^{-1}	5.64×10^{-1}	1013	936	534
M5	0.00	0.00	2.89	9.48×10^{-1}	9.48×10^{-1}	7.12×10^{-1}	1013	1013	711
M7	0.00	0.00	0.15	9.48×10^{-1}	9.48×10^{-1}	9.34×10^{-1}	1013	1013	995
M9	0.00	0.00	0.00	9.48×10^{-1}	9.48×10^{-1}	9.48×10^{-1}	1013	1013	1013

Notes. The critical altitudes, densities, and pressures are listed for an exo-Earth that is at a distance from its star such that the stellar radiation at the top of its atmosphere is identical to that received by present-day Venus, Earth, and Mars, respectively. The critical altitudes were computed on a meter-scale vertical resolution for an STP refractivity of 2.88×10^{-4} and rounded to 0.1 or 0.01 km depending on the magnitude of the critical altitude.

altitude will be slightly smaller than a simple scaling with scale height suggests. As the stellar spectral type changes from K to F, Rugheimer et al. (2013) showed that below 25 km altitudes, temperatures do not change by more than 10% (and typically far less than that, see their Figure 3), and so neither will the critical altitudes.

3.4. Effects of Different Atmospheric Composition and Planetary Sizes

Since atmospheric ray deflection depends on the composition of the atmosphere, as well as the radius of the planet (see Equation (4)), CO₂ and H₂/He dominated atmospheres are affected differently by the geometrical effect of refraction. Although the critical altitude is a useful quantity when discussing the transmission spectrum (see Section 4), it is linked to the critical density, n_c , the density that bends rays by ω_c . First, for an isothermal atmosphere, we can see from Equation (4) that

$$n_c = \frac{\omega_c}{v_{\text{STP}}(\Delta z_c)} \left(\frac{H(\Delta z_c)}{2\pi r_{\text{min}}} \right)^{1/2} = \frac{\omega_c}{v_{\text{STP}}(\Delta z_c)} \left(\frac{k_B T}{2\pi m g r_{\text{min}}} \right)^{1/2}, \quad (11)$$

where k_B is the Boltzmann constant and T , m , and g are the temperature, average molecular mass, and gravitational acceleration, respectively, of the atmosphere at r_{min} . Note that since the critical altitude is usually much smaller than the planetary radius, r_{min} can be approximated by R_p for the purpose of the following discussion. For gaseous planets, the surface planetary radius is defined at a specific pressure. Compare the critical densities of planets with identical radii with a pure CO₂ (close to Venus-like), an Earth-like, and a Jupiter-like atmosphere. Around 0.65 μm , the refractivities of H₂ and He are about 1.39×10^{-4} and 3.48×10^{-5} (Leonard 1974). Jupiter's atmosphere, composed of 86.2% H₂ and 13.6% He (Lodders & Fegley 1998), has an STP refractivity of 1.25×10^{-4} , significantly lower than the Earth's N₂/O₂ atmosphere (2.92×10^{-4}),

itself much lower than a pure CO₂ (4.48×10^{-4}) atmosphere. This difference in bending power is increased further because a H₂/He mixture has much lower average mass than a N₂/O₂ mixture, which is lighter than CO₂. Hence, CO₂ atmospheres bend light rays the most, and for a given critical deflection of a planet–star system, observers can only probe to critical densities 0.53 times that of an Earth-like atmosphere. H₂/He Jupiter-like atmospheres bend light rays the least and observers can probe denser regions with critical densities 8.3 times that of an Earth-like atmosphere. Therefore, mini-Neptunes with a H₂/He mixture can be probed to higher densities than super-Earths with a N₂/O₂ or CO₂ atmosphere, assuming similar planetary radii.

The size of a planet also has an impact on the critical density. Ignoring gravity, Equation (11) shows that a super-Earth twice the size of Earth can only be probed to a critical density 0.71 times that of the Earth. If one assumes that the solid body of the planet has a constant mass density, then the gravitational acceleration scales with the radius of the planet and $n_c \propto 1/R_p$. In this case, doubling the radius of the planet halves the critical density. Therefore, super-Earth atmospheres cannot be probed to regions as dense as Earth-sized planets. The large size of gaseous planets relative to terrestrial ones can compensate for the low bending power of H₂/He atmospheres. Factoring in the gravitational acceleration (24.8 m s⁻² for Jupiter and 9.82 m s⁻² for Earth) and the planet's radius (71,492 km for Jupiter and 6371 km for Earth), a Jupiter-sized planet with similar temperatures as the Earth can be probed down to a critical density only 1.6 times that of the Earth.

4. IMPACT OF REFRACTION ON THE TRANSMISSION SPECTRUM

To illustrate the impact that refraction has on the transmission spectrum of an exoplanet, we compute the transmission

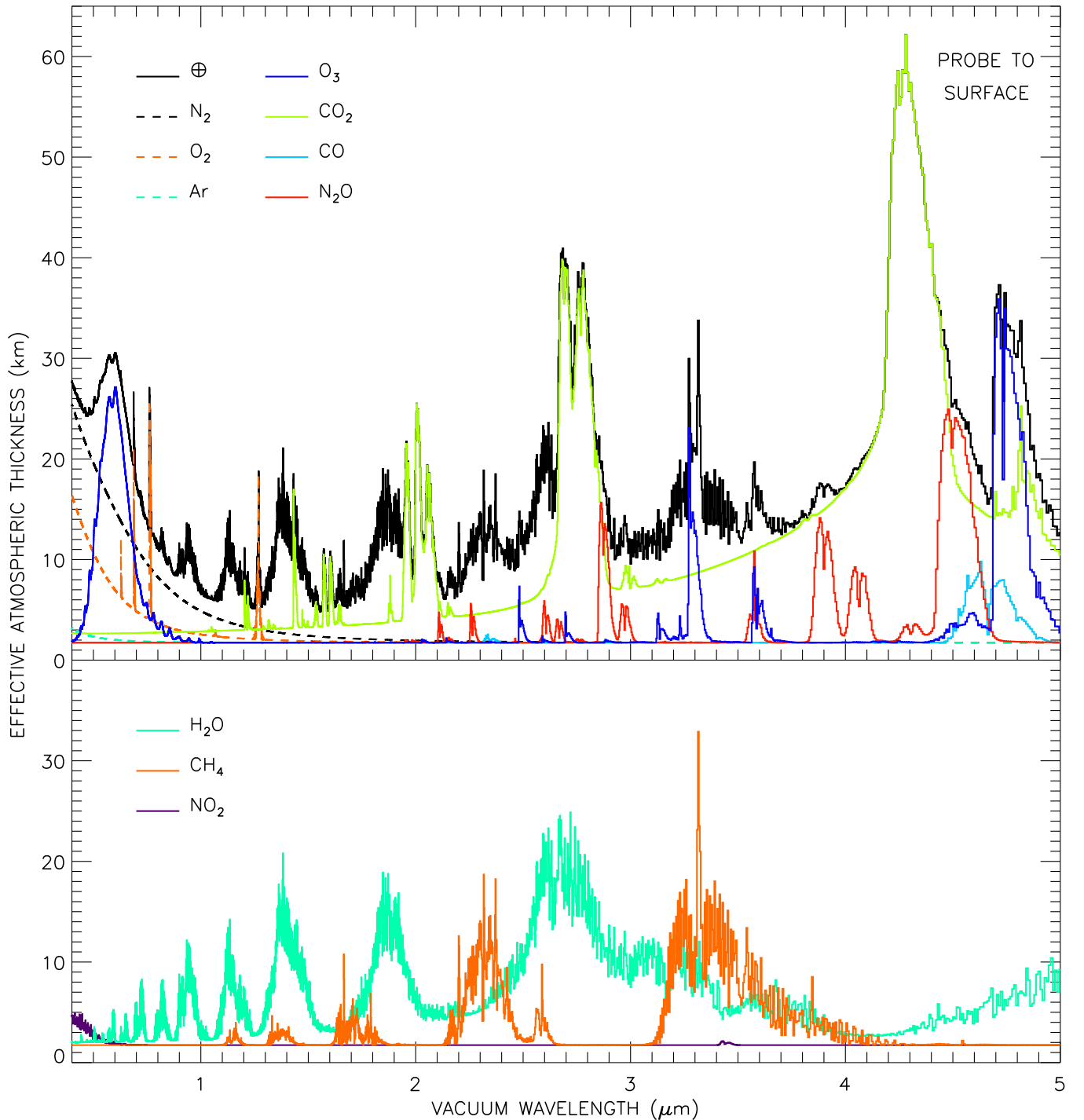


Figure 6. Transmission spectrum including the effects of refraction (solid black line) of a cloud-free transiting exo-Earth orbiting an M5–M9 star where the entire atmosphere can be probed ($\Delta z_c = 0$ km). Individual contribution from each of the important chemical species are also shown (see the legend in the upper left corner of each panel).

(A color version of this figure is available in the online journal.)

spectrum for exo-Earths orbiting different stars. We do this for exo-Earths receiving the same incident stellar flux as the Earth and divide the atmosphere into 80 layers evenly spaced in altitude from the top of the atmosphere (120 km altitude) to the critical altitude corresponding to each star (see Table 2). The bottom of each layer defines the minimum altitude reached by a ray, for which we can compute the refractivity, the impact parameter, and the transmission through the atmosphere. We compute the transmission on a 0.05 cm^{-1} grid from 2000 to $25,000 \text{ cm}^{-1}$

($0.4\text{--}5.0 \mu\text{m}$), which is then rebinned every 4.0 cm^{-1} for display. We characterize the transmission spectrum of an exo-Earth by its effective atmospheric thickness using the method described in Bétrémieux & Kaltenegger (2013), which combines the effects of atmospheric opacities and refraction.

Figure 6 shows the $0.4\text{--}5.0 \mu\text{m}$ transmission spectrum for an exo-Earth where the entire atmosphere can be probed, hence orbiting M5–M9 stars. This simulation is for a cloud-free atmosphere with an STP refractivity of 2.88×10^{-4} . The

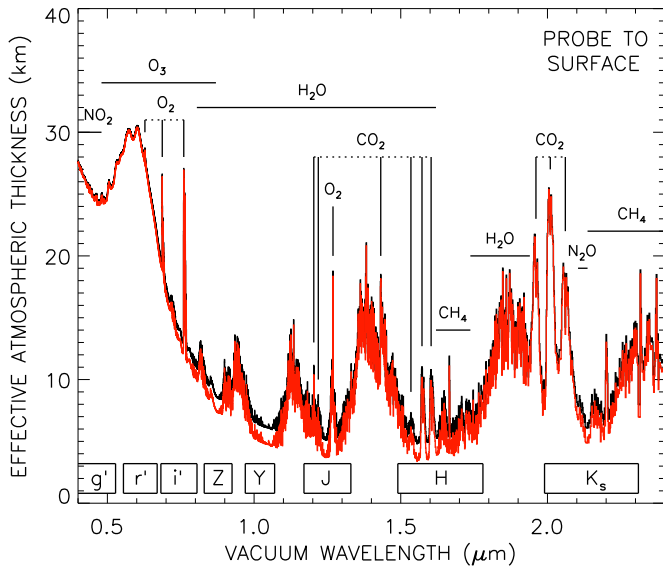


Figure 7. VIS-NIR transmission spectrum of a cloud-free transiting exo-Earth orbiting an M5–M9 star ($\Delta z_c = 0$ km) with (black line) and without (red line) refraction. Spectral regions where the spectral signatures of a molecule are prominent are identified with solid horizontal lines. Stronger individual bands of molecules are identified with solid vertical lines. Spectral coverage to the 50% transmission limit of several commonly used filters (see the text) are indicated by the black rectangles.

(A color version of this figure is available in the online journal.)

individual contribution of each species is also shown, computed by assuming that the species in question is the only one with a non-zero opacity. Note that the impact parameter of the surface lies 1.74 km above the projected surface because of the mapping of r_{\min} into b , and therefore this is the minimum value that the effective atmospheric thickness can have even in the absence of any absorption. The strongest bands in the spectrum are due to CO_2 absorption and are centered around 2.75 and 4.30 μm . A triple-band CO_2 signature (1.96–2.06 μm), as well as a few other CO_2 bands (1.20, 1.22, 1.43, 1.53, 1.57, and 1.60 μm), can be seen through the H_2O continuum. One other narrow CO_2 band centered around 4.82 μm enhances the long-wavelength side of the strongest O_3 band (4.69–4.84 μm) in the spectrum. O_3 has another strong absorption feature from 0.50–0.68 μm with a series of small bands until 1.00 μm , but these small bands are masked by H_2O features. There are a few narrow O_3 bands that can be seen above the background: a strong one at 3.27 μm , two weak ones at 2.48 and 3.13 μm , and one intermediate one blended with an N_2O band around 3.56 μm . O_2 has even fewer bands, which can be seen above the Rayleigh scattering and H_2O background at 0.69, 0.76, and 1.27 μm . N_2O has several bands blended on the long-wavelength side (2.12, 2.87, and 4.50 μm) of much stronger CO_2 bands. There are a few broad N_2O peaks in the 3.87–4.12 μm region, but the wing of the strongest CO_2 feature reduce their contrast significantly. All these features can be seen above a background composed of Rayleigh scattering (shortward of 1.3 μm), CH_4 features (1.62–1.74, 2.14–2.46, and 3.17–3.87 μm), and H_2O features (0.80–1.62, 1.74–1.94, 2.47–3.17, and 3.63–3.87 μm). Lastly, NO_2 and CO create some very weak features below 0.48 μm and 4.57–4.64 μm , respectively.

Figures 7 and 8 show the impact of refraction on the transmission spectrum of an exo-Earth orbiting an M5–M9 star for 0.4–2.4 and 2.4–5.0 μm , respectively. Figures 9 and 10 do the same but for an exo-Earth orbiting a Sun-like star. In

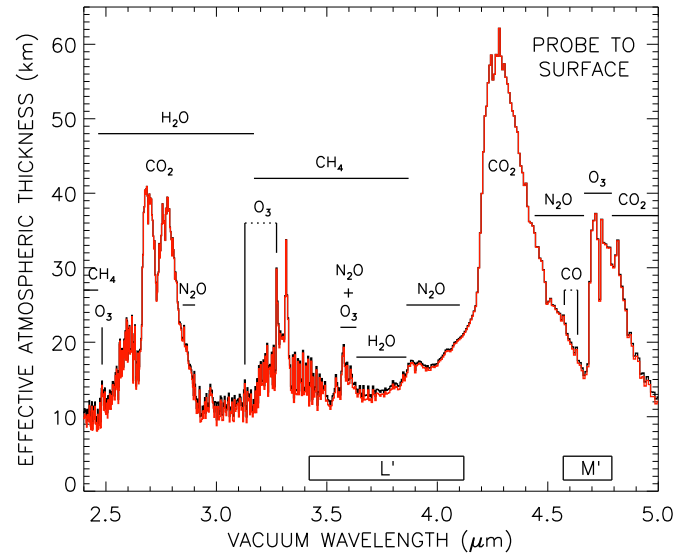


Figure 8. IR transmission spectrum of a cloud-free transiting exo-Earth orbiting an M5–M9 star ($\Delta z_c = 0$ km) with (black line) and without (red line) refraction. See the caption in Figure 7.

(A color version of this figure is available in the online journal.)

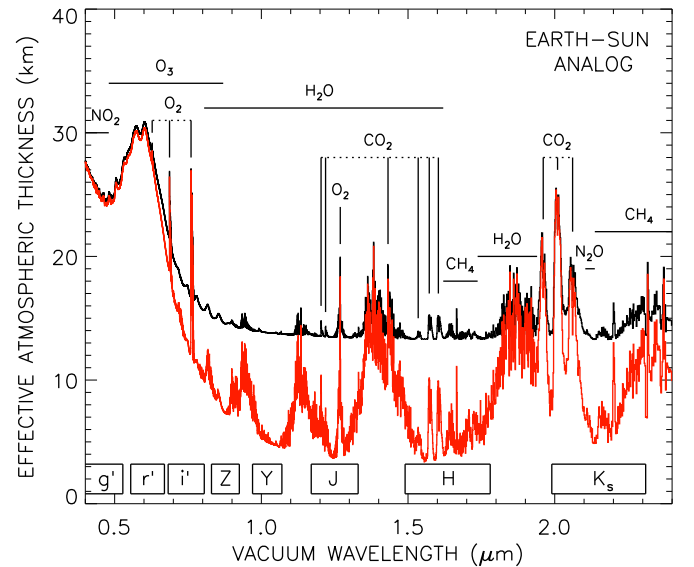


Figure 9. VIS-NIR transmission spectrum of a cloud-free transiting exo-Earth orbiting a Sun-like star ($\Delta z_c = 12.7$ km) with (black line) and without (red line) refraction. See the caption in Figure 7.

(A color version of this figure is available in the online journal.)

all four figures, the refractive properties of the atmosphere are included or not by changing the STP refractivity between 2.88×10^{-4} (black line) and 0 (red line). Note that for a refractivenessless atmosphere ($\nu_{\text{STP}} = 0$), the critical altitude is always 0 km, irrespective of the star's spectral type. For reference, the spectral coverage of a few commonly used filters in ground-based astronomy are also indicated to their 50% transmission limit (see the review by Bessell 2005). These are the g' , r' , and i' filters from the Sloan Digital Sky Survey, the Z and Y filters from the UK Infrared Deep Sky Survey, and the J, H, K_s , L' , and M' filters from the Mauna Kea Observatories.

Figures 7–10 show that for an exo-Earth, most of the interesting spectral features fall outside of the bandpass of commonly used filters from the ground, as the Earth's atmosphere is not completely transparent at these wavelengths. The Y band

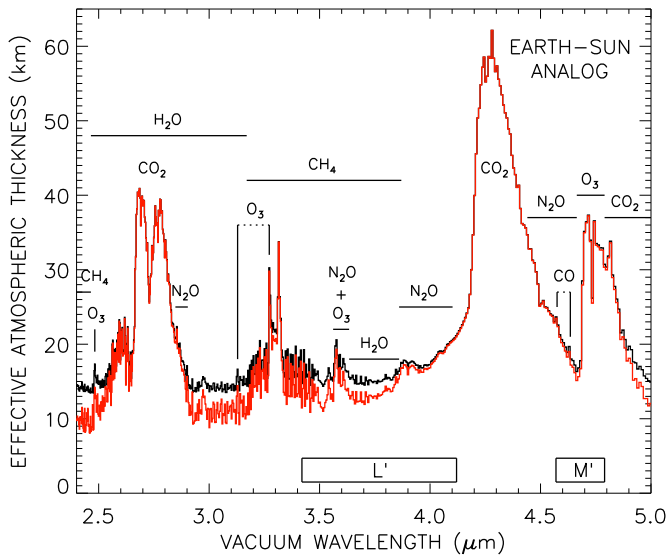


Figure 10. IR transmission spectrum of a cloud-free transiting exo-Earth orbiting a Sun-like star ($\Delta z_c = 12.7$ km) with (black line) and without (red line) refraction. See the caption in Figure 7.

(A color version of this figure is available in the online journal.)

probes a fairly featureless spectral region of an exo-Earth's transmission spectrum against which the other bands can be compared. The g' , i' , and Z bands sample the transmission spectrum where Rayleigh scattering is important (with some small contamination from other species), and the r' band can be used to look for O_3 , even in photometric mode. The M' band also catches the strongest O_3 peak, with some minor contribution from CO_2 and CO . No unambiguous information can be obtained from the other bands in photometric mode, as more than one molecule falls inside their bandpass. If spectroscopy is possible, one can look for O_2 features in both the i' and the J bands. The J band also includes CO_2 , and H_2O signatures, while the H and K_s bands cover mostly CO_2 and CH_4 signatures with a little contamination from H_2O and N_2O , respectively. The L' band samples the greatest variety of molecules: CO_2 , CH_4 , H_2O , N_2O , and O_3 .

When an exo-Earth orbits an M5 to an M9 star and the entire atmosphere can be probed (Figures 7 and 8), refraction only increases the background of the spectrum by about 1.5 km at most and the contrast in the molecular signatures are only slightly decreased. Most of the impact of refraction comes from the mapping of r_{\min} into b rather than the increase in optical depth from the ray curvature. Indeed, the difference between b and r_{\min} is 1.74, 0.94, and 0.44 km for rays reaching a minimum altitude of 0.0, 6.0, and 12.0 km, respectively. Conversely, the difference in atmospheric column abundances for these same rays is only about 7%, 4%, and 3%, respectively. Considering the atmospheric scale height, this corresponds to an altitude change of 0.62, 0.36, and 0.12 km, smaller than the respective difference between b and r_{\min} .

The geometric effect of refraction can have a much larger impact on the transmission spectrum than the other two effects. One must compare the effective atmospheric thickness of the transmission spectrum in the case where all of the atmosphere is probed against the critical altitude associated with the planet-star system. In the spectral regions where the effective atmospheric thickness is significantly larger than the critical altitude, refraction will have only minimal to no impact on the

transmission spectrum because the lower atmospheric regions are dark irrespective of refraction. Conversely, spectral regions with effective atmospheric thickness below the critical altitude will see their effective atmospheric thickness increase to the critical altitude or above, with a decrease in the contrast of spectral features as the observable column abundance of the atmosphere decreases.

In the case of an Earth-Sun analog (Figures 9 and 10) where only altitudes above 12.7 km are probed, many of the spectral features are masked or substantially reduced. Water absorption bands are severely affected as most of the H_2O is located below that altitude. Conversely, the majority of O_3 is above that altitude. Hence, shortward of about $0.89 \mu m$, all H_2O features are masked by O_3 features. Below $1.2 \mu m$, only the top of the H_2O bands around 0.94 and $1.13 \mu m$ can still be seen. Between 1.20 and $3.75 \mu m$, many of the spectral features have their contrast reduced by a factor of two to three as the effective atmospheric thickness increases to a minimum background value of 13.2 km. The CO_2 band around $2.75 \mu m$, as well as the 3.75 – $5.0 \mu m$ region, are mostly unaffected, as the atmosphere is opaque below the critical altitude.

Around hotter stars, these effects become even more pronounced. Figure 11 shows transmission spectra of exo-Earths that receive the same wavelength-integrated flux as the Earth orbiting different spectral-type stars. As the host star becomes hotter, the background of the spectrum increases and the contrast of various spectral features decreases until, for O5 stars, the hottest stars that we have considered, the exo-Earth transmission spectrum is flat with only a few remaining spectral features. Since CO_2 and O_2 are the most vertically mixed molecules with identifiable spectral features, most of their features can still be seen, albeit with a much reduced contrast. The only exceptions are the weaker CO_2 features at 1.20 , 1.22 , and $1.53 \mu m$, which become undetectable for stars hotter than B0. The strongest CO_2 bands centered at 2.75 and $4.30 \mu m$ remain quite prominent for all stars. Although all O_2 features (0.69 , 0.76 , and $1.27 \mu m$) are reduced in contrast around hotter stars, their importance relative to spectral features of other species actually increases (except for CO_2). Indeed, the nearby strong O_3 band centered at $0.59 \mu m$, which is stronger than the O_2 features for stars as hot as B5 stars, is hardly detectable for an O5 star. The weak O_3 bands below $1.00 \mu m$, as well as the weak bands at 2.48 and $3.13 \mu m$ disappear for a B0 star while the $3.56 \mu m$ O_3 band is hardly detectable around an O5 star. The stronger bands at 3.27 and around $4.76 \mu m$ are observable for all stars. The relative contribution of the CO bands around $4.60 \mu m$ increases with the temperature of the host star because CO is more abundant at altitudes above 50 km. N_2O features, which are weak throughout most of the spectrum, become undetectable around B0 host stars except for the strongest band at $4.50 \mu m$. Weaker CH_4 bands (1.62 – 1.74 , 2.14 – 2.46 , and 3.55 – $3.87 \mu m$) are much reduced in contrast around an A0 star and become undetectable around B0 stars, while the stronger CH_4 band (3.17 – $3.55 \mu m$) can be seen for all stars. H_2O bands' strengths are reduced substantially from M5 to G2 stars, and only three bands (1.35 – 1.41 , 1.80 – 1.95 , and 3.20 – $3.64 \mu m$) are still detectable around an O5 star. Finally, the slope of the spectrum shortward of $1.00 \mu m$, where Rayleigh scattering is important, changes significantly with the spectral type of the star.

The change of the transmission spectrum with stellar spectral type is due to the change of the lowest altitude probed, or the largest density and pressure probed. Although we have explored how the lowest altitude varies from the geometrical

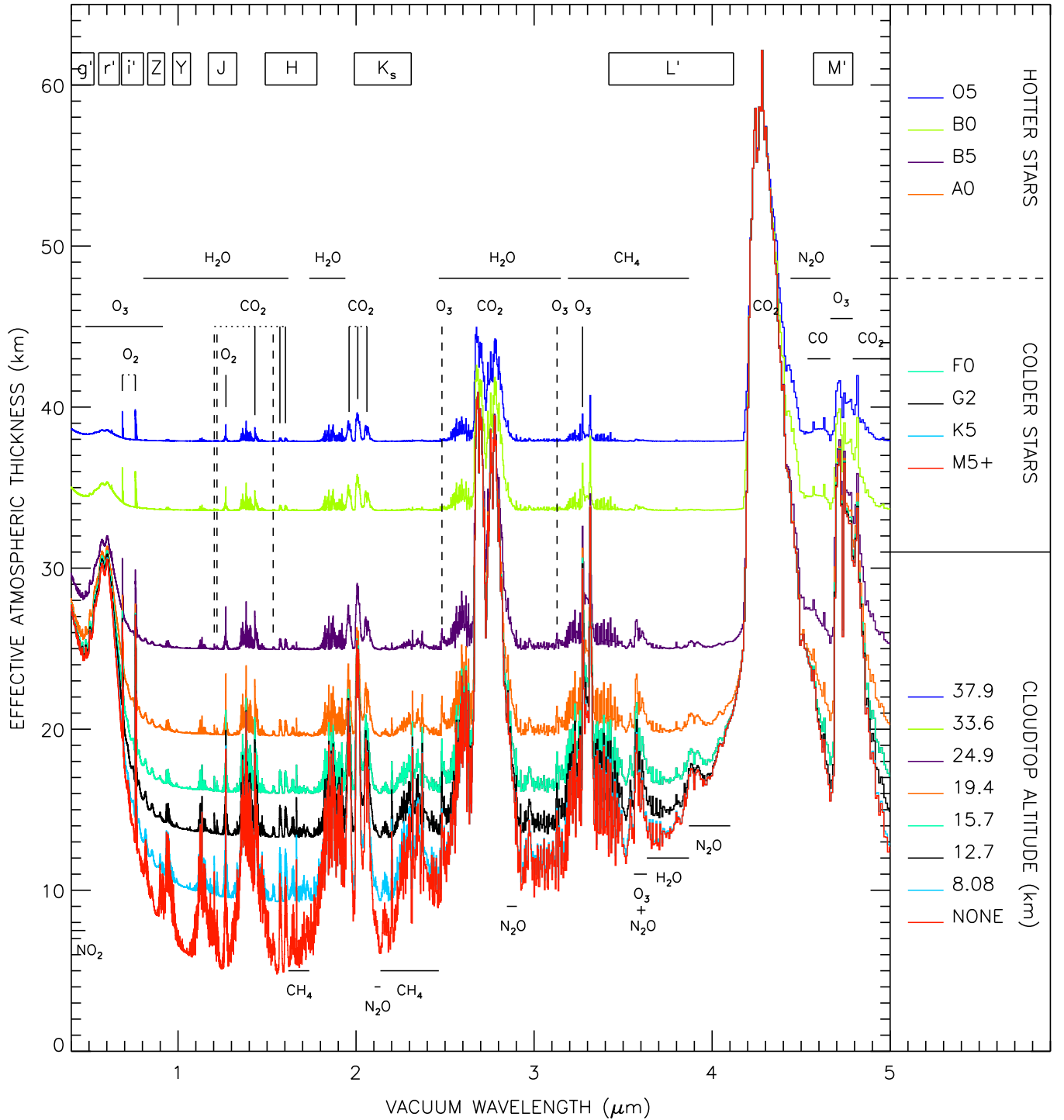


Figure 11. VIS-IR transmission spectra of a cloud-free transiting exo-Earth that receives the same wavelength-integrated stellar flux as the Earth orbiting stars of different spectral types (top right legend). A transiting exo-Earth orbiting an M5–M9 star with optically thick cloud up to the listed cloud-top altitudes (bottom right legend) produces identical transmission spectra. Regions where the spectral signatures of a molecule are prominent are identified with solid horizontal lines. Stronger individual bands of other molecules are identified with solid vertical lines except where they cannot be observed in all stellar spectral types. In the latter case, a dashed vertical line is drawn to the hottest star where they can be observed. Commonly used filters are also indicated with black rectangles.

(A color version of this figure is available in the online journal.)

effect of refraction, other limiting factors exist. The presence of optically thick clouds in this limb-viewing geometry can blanket the lower atmospheric regions and limit the lowest altitude, or highest density and pressure, probed to that of the cloud top. Hence, Figure 11 also shows the change in the transmission spectrum with the top-most altitude of a full cover of opaque clouds (see the legend). The largest density probed can also

be limited by the gas content of the atmosphere, whereby a more tenuous atmosphere will have a lower density at the surface. The largest density probed in a planet’s atmosphere is determined from the lowest value from these three causes. If the clouds are not optically thick and let some light through even in this limb-viewing geometry, then the transmission spectrum might have some exploitable signature of cloud optical properties.

If refraction is the limiting factor, lower atmospheric regions should leave some signature in the light curve profile provided that they are not opaque.

In Section 3.3, we discussed how potential temperature differences between the profile of an Earth-like planet and the Earth's atmospheric model used in this paper might impact the critical altitude. Since the transmission spectrum, expressed in terms of its effective atmospheric thickness, scales with scale height just as the critical altitude does to the first order (see Section 3.3), an increase in scale height due to temperature changes will increase the scale rather than the shape of the spectral features. The second-order effect (see Equation (11)), where higher densities can be probed with higher temperatures, implies that the background of the spectrum will decrease very slightly as the temperature increases, and this effect is much smaller than the first. Hence, as temperatures increase, we expect the spectrum to scale with planetary temperatures, accompanied by a very slight increase in the contrast of the spectral features.

5. CONCLUSIONS

Atmospheric refraction plays a major role in transmission spectroscopy of habitable exoplanets. The geometric effect of refraction limits how deeply observers can probe a planet's atmospheres. The angular size of the host star with respect to the exoplanet, and to a lesser extent the size of the exoplanet itself, determines the critical deflection by which a ray can be bent and still reach the observer. Comparison of this critical deflection against the vertical bending properties of the atmosphere defines a critical altitude below which, and a critical density and pressure above which, the atmosphere cannot be probed. When the critical deflection is larger than the deflection at the surface of the planet, observers can probe the atmosphere down to the surface. In a first-order approximation, the critical deflection scales with $1/T_*^2$ (effective temperature of the host star) for exoplanets with identical incident stellar flux on the top of their atmospheres. Thus, observers can probe deeper in the atmosphere of planets orbiting cooler stars for a given atmospheric profile.

The critical altitude and density depend on the composition of the atmosphere. CO₂ bends light more than an Earth-like N₂/O₂ atmosphere, and a Jupiter-like H₂/He atmosphere bends light the least. The large radius of gaseous giants can mitigate that effect. Also, super-Earths cannot be probed to densities as high as those on Earth-sized planets or on mini-Neptunes.

We determined the critical altitudes, densities, and pressures for exoplanets with identical mass, radius, and 1 bar N₂/O₂ atmosphere as the Earth, which receive the same incident stellar fluxes as Mars, Earth, and Venus, orbiting various stars from O5 to M9 spectral type. The hottest star around which all of this exo-Earth's atmosphere can be probed is an M1, M4, and M7, for the same incident stellar flux as Venus, Earth, and Mars, respectively. Transmission variability cannot be caused

by clouds if the critical altitude is greater than the altitude of the topmost clouds. For an exo-Earth with an Earth-like incident stellar flux, this occurs around stars like the Sun or hotter.

We illustrated the impact of refraction on the 0.4–5.0 μm transmission spectrum of an exo-Earth receiving the same incident stellar flux as Earth orbiting O5 to M9 stars. As the critical altitude increases, the spectrum's background increases, decreasing the contrast of spectral features or masking them entirely. If an exo-Earth can exist around an O5 star, its transmission spectrum would be sparsely populated with only the strongest CO₂, H₂O, O₂, O₃, CH₄, CO, and N₂O bands, but would be otherwise flat, in stark contrast to that around M5 to M9 stars. The strongest bands are the 2.75 and 4.30 μm CO₂ bands and the 4.76 μm O₃ band. Whether the lowest altitude that can be probed is due to the refraction effect, the presence of optically thick clouds in a limb-viewing geometry extending to the same altitude, or a surface at the corresponding pressure makes no difference to the transmission spectrum. Hence, the geometrical effect of refraction is another phenomenon that can potentially explain flat transmission spectra.

The authors acknowledge support from DFG funding ENP Ka 3142/1-1 and the Simons Foundation (290357, Kaltenegger).

REFERENCES

- Benneke, B., & Seager, S. 2012, *ApJ*, **753**, 100
 Bessell, M. S. 2005, *ARA&A*, **43**, 293
 Bétrémieux, Y., & Kaltenegger, L. 2013, *ApJL*, **772**, L31
 Cox, A. N. 2000, *Allen's Astrophysical Quantities* (4th ed.; New York: AIP)
 Csizmadia, Sz., Pasternacki, Th., Dreyer, C., et al. 2013, *A&A*, **549**, A9
 Ehrenreich, D., Tinetti, G., Lecavelier des Etangs, A., Vidal-Madjar, A., & Selsis, F. 2006, *A&A*, **448**, 379
 García Muñoz, A., & Mills, F. P. 2012, *A&A*, **547**, A22
 García Muñoz, A., Zapatero Osorio, M. R., Barrena, R., et al. 2012, *ApJ*, **755**, 103
 Goldsmith, W. W. 1963, *Icar*, **2**, 341
 Hedelt, P., von Paris, P., Godolt, M., et al. 2013, *A&A*, **553**, A9
 Hubbard, W. B., Fortney, J. J., Lunine, J. I., et al. 2001, *ApJ*, **560**, 413
 Kaltenegger, L., & Traub, W. A. 2009, *ApJ*, **698**, 519
 Leonard, P. J. 1974, *ADNDT*, **14**, 21
 Lodders, K., & Fegley, B., Jr. 1998, *The Planetary Scientist's Companion* (New York: Oxford Univ. Press)
 Misra, A., Meadows, V., Claire, M., & Crisp, D. 2014, *AsBio*, **14**, 67
 Pallé, E., Zapatero Osorio, M. R., Barrena, R., Montañés-Rodríguez, P., & Martín, E. L. 2009, *Natur*, **459**, 814
 Rauer, H., Gebauer, S., von Paris, P., et al. 2011, *A&A*, **529**, A8
 Reid, I. N., & Hawley, S. L. 2005, in *New Light on Dark Stars: Red Dwarfs, Low-Mass Stars, Brown Dwarfs*, ed. I. N. Reid & S. L. Hawley (New York: Springer-Praxis), 169
 Rodler, F., & López-Morales, M. 2014, *ApJ*, **781**, 54
 Rugheimer, S., Kaltenegger, L., Zsom, A., Segura, A., & Sasselov, D. 2013, *AsBio*, **13**, 251
 Sidis, O., & Sari, R. 2010, *ApJ*, **720**, 904
 Smith, G. R., & Huxten, D. M. 1990, *RvGeo*, **28**, 117
 Snellen, I., de Kok, R., Le Poole, R., Brogi, M., & Birkby, J. 2013, *ApJ*, **764**, 182
 Vidal-Madjar, A., Arnold, A., Ehrenreich, D., et al. 2010, *A&A*, **523**, A57